Green Chemistry

PAPER

View Article Online
View Journal | View Issue

Cite this: *Green Chem.*, 2025, **27**, 6813

Mechanochemical approach to polymer-functionalized black phosphorus nanomaterials for precious metal recovery†

Obida Bawadkji, [a] Peng Tang,[a] Christian Müller*[b] and Rainer Haag *[a]

Received 16th January 2025,
Accepted 2nd May 2025

DOI: 10.1039/d5gc00274e

rsc.li/greenchem

Rapid and sustainable methods for precious metal recovery are urgently needed to support circular economy initiatives. Herein, we introduce a one-pot mechanochemical route to synthesize a black phosphorus–polyglycerol (BP–PG) nanohybrid with enhanced interfacial reactivity for selective gold ion reduction. The process transforms inexpensive red phosphorus directly into amorphous BP and, subsequently, into BP–PG *via* planetary ball milling, thereby eliminating high temperatures, extended reaction times, and toxic solvents commonly used in conventional functionalized-BP nanomaterial syntheses. This "grafting-from" polymerization of glycidol onto BP yields a uniform, hydrophilic hybrid that can rapidly and selectively reduce gold ions to stabilized gold nanoparticles. Notably, BP–PG recovers more than three times its own weight in gold, far surpassing previously reported materials, while leveraging a scalable, cost-effective, and green production method. These findings underscore the critical role of synthetic strategy and material architecture in achieving high-performance nanohybrids, offering promising opportunities for precious metal recovery and broader interface-driven applications.

Green foundation

1. We developed a solvent-free, mechanochemical route to synthesize a black phosphorus–polyglycerol nanohybrid, effectively eliminating harmful solvents and reducing energy use and reaction times, for the recovery of gold from e-waste. This method aligns with green chemistry principles by promoting resource recovery while minimizing environmental impact through selective recovery of precious metals.
2. Our key achievement is a one-pot synthesis that circumvents toxic solvents, requires no high-temperature chemical vapor transport, and achieves remarkable gold uptake, exceeding three times the material's weight. The resulting biodegradable nanohybrid prevents long-term ecological harm.
3. Future efforts could focus on scaling up ball-milling process and adopting bio-based glycidol sources. Although mechanochemistry offers scalability potential, further research could explore optimizing the mechanochemical process to enhance throughput. Moreover, investigating the use of bio-derived precursors for glycidol could improve the sustainability of the starting materials.

Introduction

The increase in global electronic waste and mining activities necessitates sustainable methods to recover precious metals like gold, palladium, and platinum from electronic waste leachate and mining wastewater.[1–7] These metals are extensively used in industries such as electronics, catalysts, and jewelry, resulting in waste containing complex mixtures of precious metals and toxic contaminants.[8] Traditional hydrometallurgical processes use leaching agents like cyanide and involve recovery techniques such as electrodeposition and solvent extraction but are limited by high costs and hazardous byproducts.[9–12] They also tend to produce bulk gold, which requires additional processing steps to obtain gold nanoparticles of catalytic or biomedical importance.[3]

Black phosphorus (BP) nanomaterials provide a sustainable and efficient solution for recovering and reducing gold ions due to their high surface area and abundant active sites for metal ion adsorption.[13–17] Phosphorus atoms in BP reduce gold ions (Au^{3+}) to elemental gold (Au^0) under mild conditions without external reducing agents, leading to the spontaneous formation of gold nanoparticles on BP nanosheets.[14,15] This dual functionality simplifies the recovery process and reduces chemical consumption, making it environmentally friendly and cost-efficient.[15] BP is also biodegradable, degrading into benign phosphates,[18,19] and it exhibits high selectivity for gold ions over other metals.[14,15] Zhang *et al.* functionalized black phosphorus with poly(*N*-iso-

[a]*Institut für Chemie und Biochemie, Freie Universität Berlin, Takustr. 3, 14195 Berlin, Germany. E-mail: haag@zedat.fu-berlin.de*
[b]*Institut für Chemie und Biochemie, Freie Universität Berlin, Fabeckstr. 34/36, 14195 Berlin, Germany. E-mail: c.mueller@fu-berlin.de*

†Electronic supplementary information (ESI) available. See DOI: https://doi.org/10.1039/d5gc00274e

propylacrylamide) (PNIPAM) to create a responsive material (BP–P) that enables rapid, highly selective extraction of precious metals like gold, silver, and palladium under mild conditions, with potential applications in hydrogen evolution reactions.[15,20]

However, current methods for producing BP nanomaterials face significant limitations such as high cost, complexity, toxicity, and lack of scalability. Typically, BP nanomaterials are derived from liquid exfoliation of BP crystals produced *via* the expensive, toxic, and non-scalable chemical vapor transport (CVT) method, which utilizes heavy-metal iodides, costs 570–700 € per g and requires over 18 hours to complete.[21–23] Producing and functionalizing BP nanomaterials involves further steps like mechanical crushing and ultrasonication in toxic solvents, use of hazardous activating agents, and requires costly purification procedures.[24–26] Alternative solvothermal techniques have been developed but are also economically and ecologically non-feasible due to the use of toxic materials and are suitable only for obtaining small amounts of BP.[27,28] Additionally, pure BP nanomaterials aggregate in aqueous solutions,[29] so they require covalent functionalization with hydrophilic materials like polyglycerol (PG).[26,30,31] However, polymer functionalization is typically achieved through challenging, costly, and often toxic solvent-based methods.[15,26,31] These processes encapsulate the nanomaterial, limiting its interaction with surroundings and reducing performance in interfacial applications.[18,26,32] Exfoliating expensive BP crystals using techniques like sonication yields low amounts of few-layered nanosheets with minimal defects and pores, resulting in a lower surface area compared to amorphous structures.[24,26] Gold nucleation on BP nanosheets primarily occurs at defects or edges, promoting the growth of gold nanoparticles.[14,33] While BP nanosheets can be fixed onto solids with higher surface areas, such as covalent organic frameworks or porous spherical montmorillonite, this adds expense and complexity to the functionalization process.[34,35]

A more sustainable, green, and rapid method for producing functional BP nanomaterials is mechanochemistry.[36,37] In the context of BP synthesis, mechanochemical methods enable the direct transformation of RP into BP under ambient conditions.[38–46] eliminating the need for high temperatures, high pressures, toxic reagents, enhances energy efficiency, significantly reduces synthesis times, and allows better control over particle size and crystallinity, which is crucial for high-quality BP materials.[38–40,46] Regarding BP nanomaterial production, mechanochemical processes under the right conditions can directly form nanomaterials without further processing, addressing challenges of traditional exfoliation techniques,[46] as well as allowing subsequent surface functionalization to improve BP's dispersibility in aqueous solutions and stability under ambient conditions, enhancing its performance in various applications.[32]

Here, we introduce a solventless, mechanochemically synthesized black phosphorus–polyglycerol (BP–PG) nanohybrid as a high-capacity selective precious metal recovery agent (Fig. 1). This rapid, eco-friendly method aligns with green chemistry principles, and the biodegradability of black phosphorus ensures minimal environmental impact.[47–49] This work

Fig. 1 BP–PG as a recovery agent for Au from electronic waste, contributing to a circular economy. AI-generated nanomaterial image.

pioneers the first successful mechanochemical polymerization of glycidol into polyglycerol using a "grafting-from" technique, representing an advancement in mechanochemical polymerizations as low-functional liquid epoxides do not polymerize so easily mechanochemically.[50] Our approach creates a true nanohybrid by combining a solid inorganic nanomaterial (BP) with a liquid organic nanomaterial (PG) in a one-pot process starting from red phosphorus (RP) and glycidol, both relatively inexpensive starting materials.[51,52] The resulting highly hydrophilic nanomaterial is ideal for aqueous environments. BP serves as an efficient gold-reducing agent, while PG functions as both a stabilizer for gold nanoparticles (AuNPs) and a hydrophilic component that ensures uniform distribution and prevents aggregation.[53] Previous syntheses relied on toxic solvents and suffered from low yields and time-consuming purification.[26] In contrast, our solventless approach retains both components' properties, enabling selective recovery of gold ions under complex acidic conditions and directly producing mesodisperse stabilized AuNPs.

Results & discussion

Synthesis and characterization of BP and BP–PG

The benefits of mechanochemically obtained BP–PG, utilizing high-energy planetary ball-milling (HEPBM) as the mechanochemical method, were thoroughly assessed in comparison to nanoparticles obtained *via* a traditional solvent-based approach (BP@PG), previously reported by our group (Fig. 2a).[26] Motivated by the limitations of traditional BP syn-

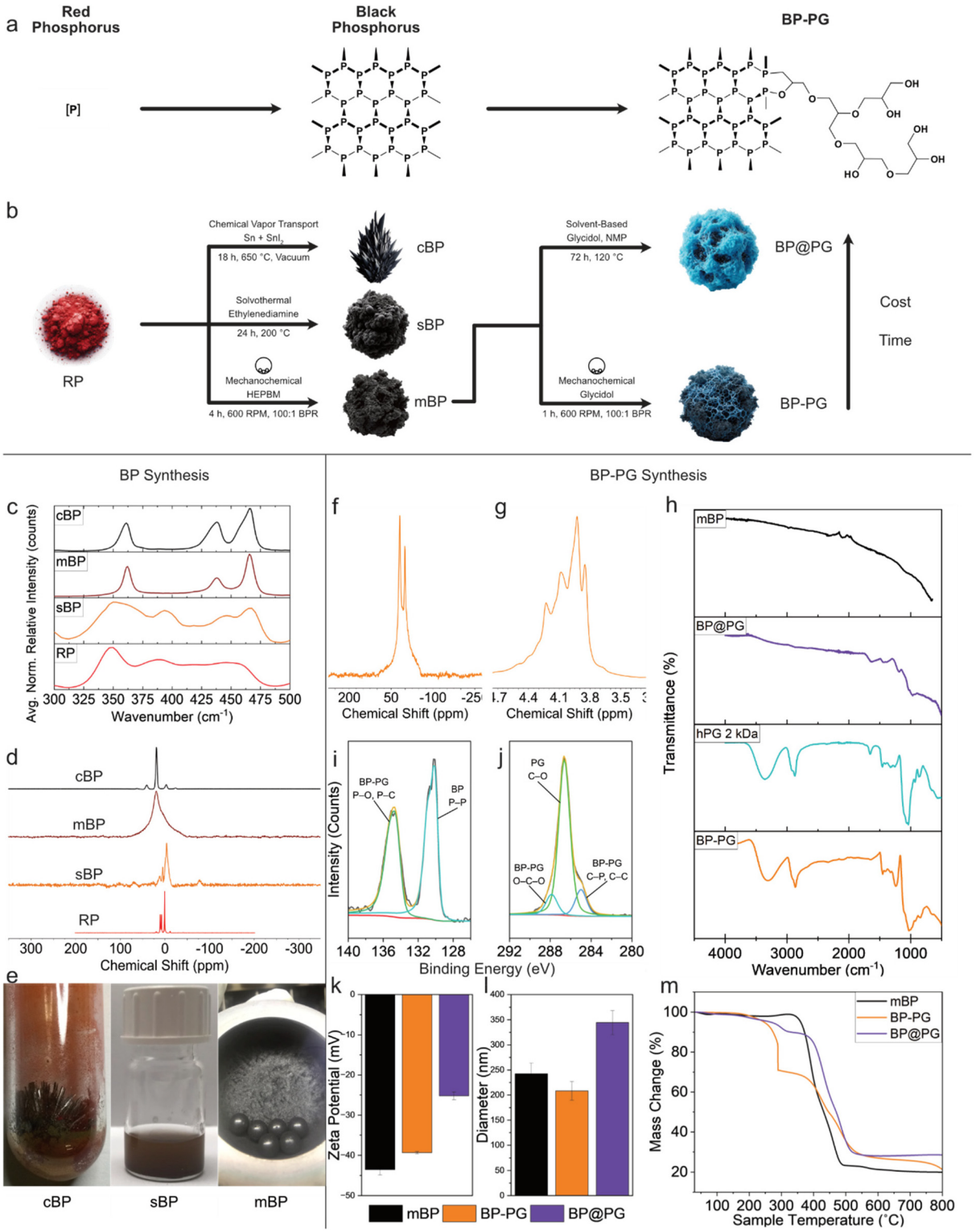

Fig. 2 (a) Scheme and (b) overview of the nanomaterials in this study. (c) Average normalized spectra derived from Raman maps and (d) ^{31}P-MAS-NMR spectra obtained from analysis of RP, mBP, cBP, and sBP showing the high quality of the mechanochemically produced mBP. (e) Images of cBP, sBP, and mBP. Spectroscopic characterization of BP–PG and/or BP@PG by (f) ^{31}P-MAS-NMR, (g) ^{1}H-NMR, (h) FT-IR, and hi-res (i) P2p and (j) C1s XPS, all indicating a high degree of functionalization. (k) ZP, (l) DLS, and (m) TG measurements of mBP, BP–PG, and BP@PG. AI-generated nanomaterial image.

thesis methods, we aimed to develop a more efficient and environmentally friendly approach for producing BP nanoparticles. We adopted a mechanochemical synthesis involving planetary ball milling of red phosphorus under an inert atmosphere, facilitating the conversion to black phosphorus through continuous mechanical activation. Subsequently, the produced BP was functionalized with PG *via* a mechanochemical process, yielding BP–PG nanohybrids with enhanced surface area and improved dispersibility. To assess the quality and potential advantages of the mechanochemically synthesized BP nanoparticles (mBP), we systematically compared them with BP nanoparticles obtained *via* solvothermal (sBP) and chemical vapor transport (cBP) methods. This comparison was conducted using Raman spectroscopy, phosphorus magic angle spinning solid-state nuclear magnetic resonance (^{31}P-MAS-NMR), and powder X-ray diffraction (PXRD).

Although mechanochemical methods have shown promise as a green and cost-effective route to black phosphorus, achieving consistently high-quality yields and large-scale production remains an active area of research.[39,40,54] Therefore, obtaining sufficient amounts of high-quality BP within a reasonable processing time *via* a green, non-expensive and facile method is a key requirement for achieving realistic implementation of BP for different applications. To obtain high quality BP mechanochemically within a reasonable amount of time, a relatively high ball-to-powder ratio (BPR) of >25 : 1 is necessary (Fig. 2b and ESI 1†). Depending on the available ball-mill apparatus, gram-scale yields of high-quality BP nanoparticles can be obtained within a few-hour of milling time (Fig. 2e). The Raman spectrum of the formed BP nanoparticles (mBP) using HEPBM shows a high allotropic conversion mainly seen by the pronounced generation of the B_{2g} and the A_g^2 black phosphorus vibrational peaks at 435 cm^{-1} and 463 cm^{-1}, respectively, and the strong depletion of the broad band between 368–425 cm^{-1}. Additionally, a blue shift of the B_1 red phosphorus peak at 350 cm^{-1} to the A_g^1 black phosphorus peak at ~360 cm^{-1} (Fig. 2c and ESI 1†) can be observed, which closely resembles the vibrational bands of cBP obtained *via* CVT. Comparatively, these vibrational features from sBP are not clearly indicated even after heating at 170 °C. Raman maps obtained from mBP show a narrow distribution of the BP Raman vibrational bands (ESI 1†), which indicates an exceptional uniformity in quality. Moreover, dynamic light scattering spectroscopy (DLS) of an mBP dispersion (Fig. 2l) reveals nano-sized particles. We therefore anticipate that our suggested mechanochemical approach can produce high-quality mBP nanoparticles in a single step. Although the CVT method resulted in a high allotropic conversion for cBP, the solvent-based exfoliation did not produce BP nanoparticles with a uniform morphology, which can be concluded by the broader distribution of Raman vibrational bands in the acquired Raman map (Fig. 2c and ESI 1†). In such a procedure, it is typical to separate the bulky particles from the exfoliated nanoparticles *via* centrifugation, which leads to a high loss in BP yield.[26] The Raman map from sBP reveals a low allotropic conversion, which can be attributed to the hindered access of the ethylenediamine solvent to the inner core of the RP particles throughout the synthesis, leading to an allotropic conversion mostly on the surface of the treated particles (Fig. 2c and ESI 1†). Likewise, ^{31}P-MAS-NMR spectroscopy of sBP indicates a heterostructure of red and black phosphorus, whereas mBP shows a clear single broad signal at δ = ~19.0 ppm, that indicates amorphous BP (Fig. 2d). The amorphous nanoparticle morphology of the produced mBP, which results from the process of HEPBM, is also obvious by the lack of diffraction pattern of BP, which are present in the layered crystal structure of cBP (ESI 1†). This amorphous morphology is desired for its application as a recovery agent, as the surface area is higher than that of few-layer BP nanosheets.

Considering the high quality of the produced BP nanoparticles, which were obtained in a quick, facile, and environmentally friendly approach, mBP was used for further functionalization with PG (Fig. 2a and b). The benefits of mechanochemically produced BP–PG were assessed in terms of synthesis, hybridity of properties, environmental-friendliness, production cost, and its ability to selectively recover gold in the form of AuNPs with a high recovery capacity from an ionic mixture of metals.

BP–PG was obtained *via* a HEPBM approach by combining a 1 : 1 w/w ratio of mBP and glycidol in a stainless-steel chamber together with a stainless-steel ball-mill medium and treating both reagents at a high milling energy under inert atmosphere. Thus, BP–PG can be obtained in a one-pot two-step process starting from only RP and glycidol. On the other hand, BP@PG was obtained by adapting a similar procedure previously reported from our research group, but using the same produced mBP and mBP/glycidol w/w ratio of 1 : 1 for a comparative assessment.[26] Both reagents were dispersed in NMP and treated at 120 °C for 72 hours under inert atmosphere before purification of the nanoparticles to finally obtain BP@PG. Regarding BP–PG, a successful polymerization of glycidol to PG and functionalization of the BP nanoparticles can occur within 15 minutes at high milling energies as seen by the development of the polyglycerol multiplet between δ = 3.4–4.0 ppm in the ^{1}H-NMR spectra[55] (Fig. 2g amd ESI 2b†), whereas only a weak signal appears for PG even after 72 hours of heating at high temperatures (ESI 2a†). ^{31}P-MAS-NMR shows a sharp intense signal at δ = ~0.0 ppm, that indicates P–O bonds arising from a high-degree functionalization of BP by glycidol monomers which polymerized onto BP nanoparticles (Fig. 2f). BP@PG, however, was functionalized to a much lesser degree as indicated by a very broad signal around δ = ~0.0–10.0 ppm, which is typical for P_xO_y species (ESI 2c†). Fourier transform infrared spectroscopy (FT-IR) reveals intense signals for BP–PG at 1240 cm^{-1} and 978 cm^{-1}, that corresponds to the P–O–C asymmetric and symmetric stretches, respectively, as well as all the characteristic PG stretches for the O–H, C–H, and C–O–C bonds at 3000–3600 cm^{-1}, 2877 cm^{-1}, and 1045 cm^{-1}, respectively (Fig. 2h).[55] These signals are not noticeable for BP@PG. Similarly, Raman vibrational bands for BP@PG are relatively attenuated in comparison to BP and BP–PG as seen by the broadness of the A_g^1,

B_{2g}, A_g^2 peaks (ESI 2d†) because the polymer coverage scatters the incoming laser light and absorbs part of the scattered Raman light. The X-ray photoelectron spectroscopy (XPS) P2p spectrum shows P–P bonds from the BP component at 130–131 eV and P–O and P–C bonds from the BP–PG covalent functionalization at 134–135 eV (Fig. 2I and ESI 3†). The C1s spectrum (Fig. 2j and ESI 3†) indicates C–O bonds mainly from the PG component at 286 eV and C–P and O–C–O bonds from the BP–PG covalent functionalization at 284 eV and 287 eV, respectively. On the other hand, XPS analysis of BP@PG revealed functionalization to a lesser degree indicated by the smaller P–O and P–C peak in the P2p spectrum (ESI 3†), and a smaller C–O peak in the C1s spectrum. This is also indicated by the higher carbon-to-phosphorus atomic ratio derived from the survey spectra (ESI 3†) of BP–PG (~4.72) as compared to that of BP@PG (0.32). Based on our results, we propose that the epoxide ring of glycidol undergoes nucleophilic ring-opening by the phosphorus atoms in BP, initially forming P–C bonds. Subsequently, the oxygen sites of the growing polyglycerol chains can further react with BP to establish additional P–O linkages, thereby building the integrated BP–PG network.

Varying the BP-to-glycidol weight ratio, especially by reducing it, in the mechanochemical process hindered successful polymerization into polyglycerol-functionalized BP nanoparticles (ESI 4a and c†). This likely resulted from insufficient BP substrate, as glycidol, a low-molecular-weight liquid epoxide, could require ample reactive surface sites, like those on BP, to initiate polymerization effectively. The resulting products were characterized by FTIR and ^{1}H-NMR, revealing that sufficient BP surface is essential for an effective mechanochemical ring-opening of glycidol, which otherwise remains largely unpolymerized at high glycidol/bulk BP ratios. Conversely, a very high BP content can limit polyglycerol formation, affecting the final materials' dispersibility and performance.

Regarding production time, the mechanochemical approach can be used for both a rapid allotropic conversion of BP and a high-degree functionalization with PG *via* anion ring opening polymerization of glycidol in a one-pot two-step process, standing out as the favorable approach in practical scenarios (Fig. 3). Attempting a single-step reaction between RP and glycidol lead to various chemical species different than that obtained by the 2-step approach that yields BP–PG (ESI 4b and d†), likely due to various side reactions between RP and glycidol that hinder the allotropic transformation of RP to BP and its functionalization with polyglycerol thereafter.

Physicochemical properties of BP–PG

After the successful functionalization and homogeneous distribution of BP–PG's molecular components, we were interested in investigating the properties of both BP and PG. The zeta potential (ZP) measurements reveal a negative charge of −43.5 mV for BP and −39.4 mV for BP–PG, which is mainly due to the presence of phosphorus lone-pairs in the BP

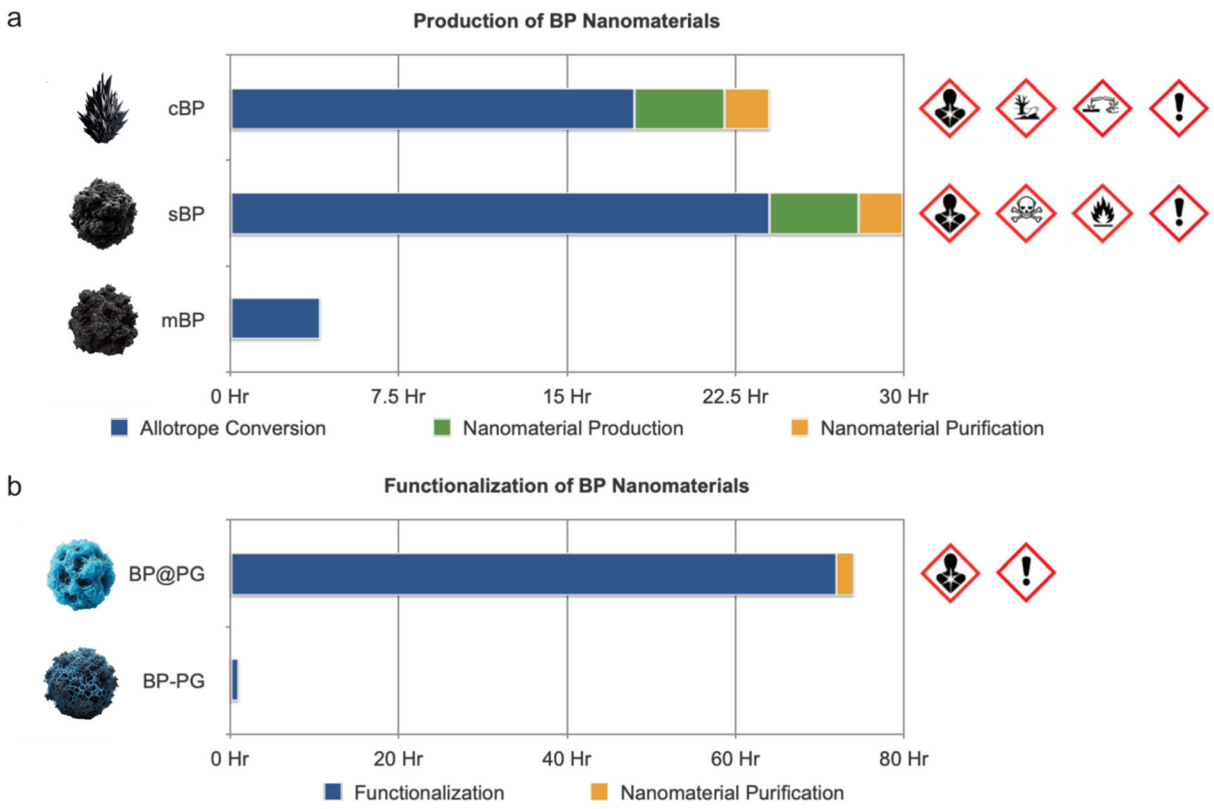

Fig. 3 Production time and GHS safety symbols accompanying reagents (apart from RP and glycidol) required to produce (a) cBP, sBP, mBP, (b) BP@PG, and BP–PG. The total time to produce BP–PG mechanochemically is approximately 5 hours. AI-generated nanomaterial image.

(Fig. 2k). On the other hand, the surface coverage that decorates BP@PG that results from the solvent-based approach, diminishes this negative charge and is only −25.2 mV, which can lead to aggregation of the nanoparticles as the negative repulsive forces are not strong enough to keep the nanoparticles dispersed in aqueous environments. Indeed, DLS analysis reveals a greater diameter of 344 nm for BP@PG that results from aggregation as compared to 208 nm for BP–PG (Fig. 2l). The more negative surface charge of BP–PG indicates a higher concentration of BP on the nanoparticle surface. This increased surface of BP in BP–PG, compared to its solvent-based polymer-encapsulated counterpart BP@PG, enhances its effectiveness, as the high negative surface charge exhibits improved stability in suspension due to stronger electrostatic repulsion, which helps prevent aggregation.[25] This allows for greater surface availability, making BP–PG more effective for interactions with target ions, such as in ion recovery and adsorption applications.[56,57] Regarding the dispersibility of the nanomaterials in aqueous systems, both BP–PG and BP@PG reveal higher dispersibility as compared to bare mBP

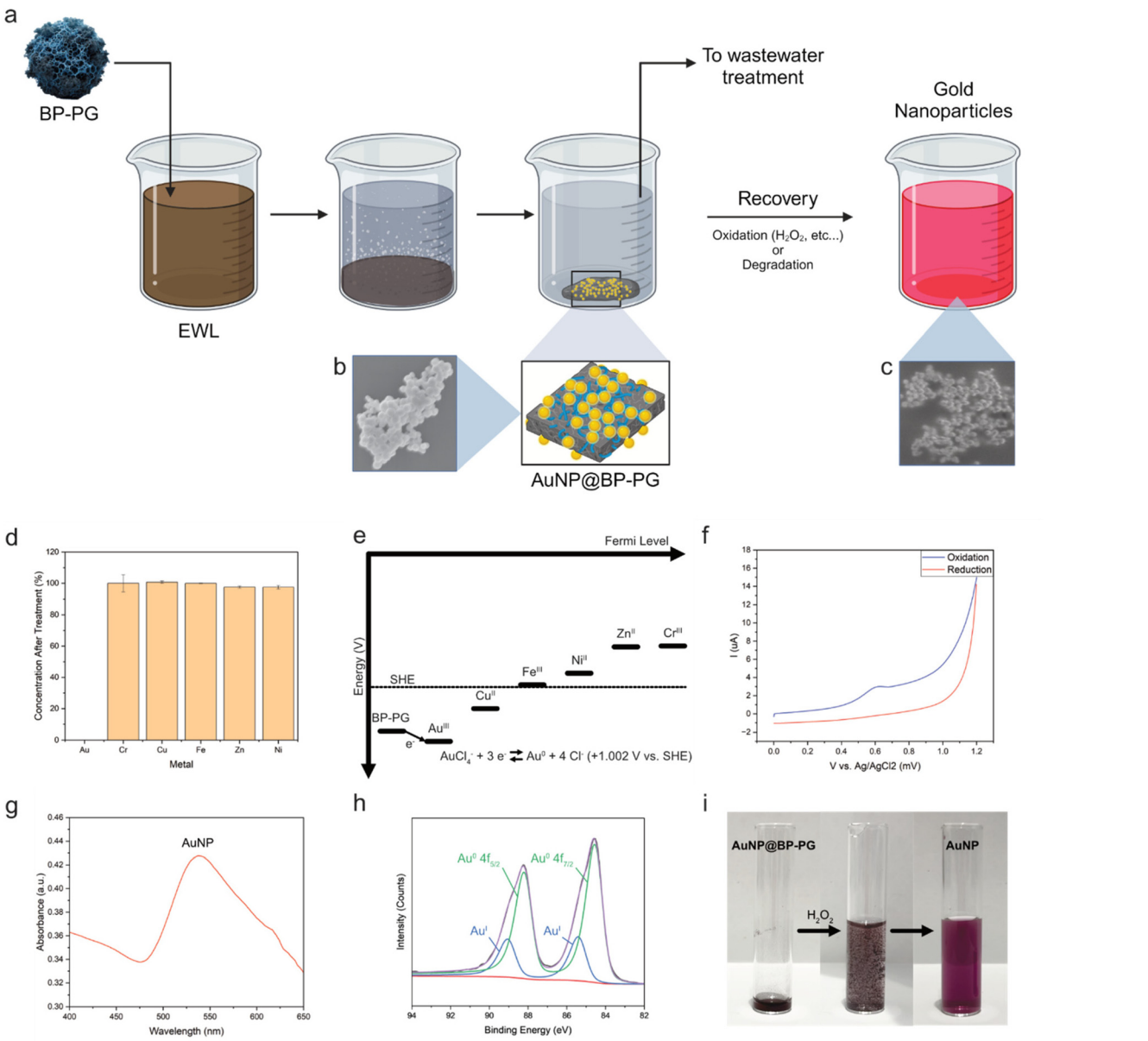

Fig. 4 (a) Overall scheme of AuNP production and recovery from EWL treated with BP–PG. SEM images of (b) AuNP@BP–PG and (c) AuNPs recovered from BP–PG. (d) AAS analysis of metals present in solution after treatment with BP–PG indicating high selectivity for Au. (e) Work functions of the metals in EWL giving insight to the selective BP–PG/$AuCl^{4-}$ redox pair formation.[63] (f) CV analysis of BP–PG showing irreversible oxidation of the nanomaterial. (g) UV-Vis and (h) Au 4f XPS analysis of the AuNPs formed from treatment of EWL with BP–PG, both indicating reduced zero-valent Au species. (i) Treatment of AuNP@BP–PG with H_2O_2 to oxidize the BP–PG component to finally recover the AuNPs. AI-generated nanomaterial image.

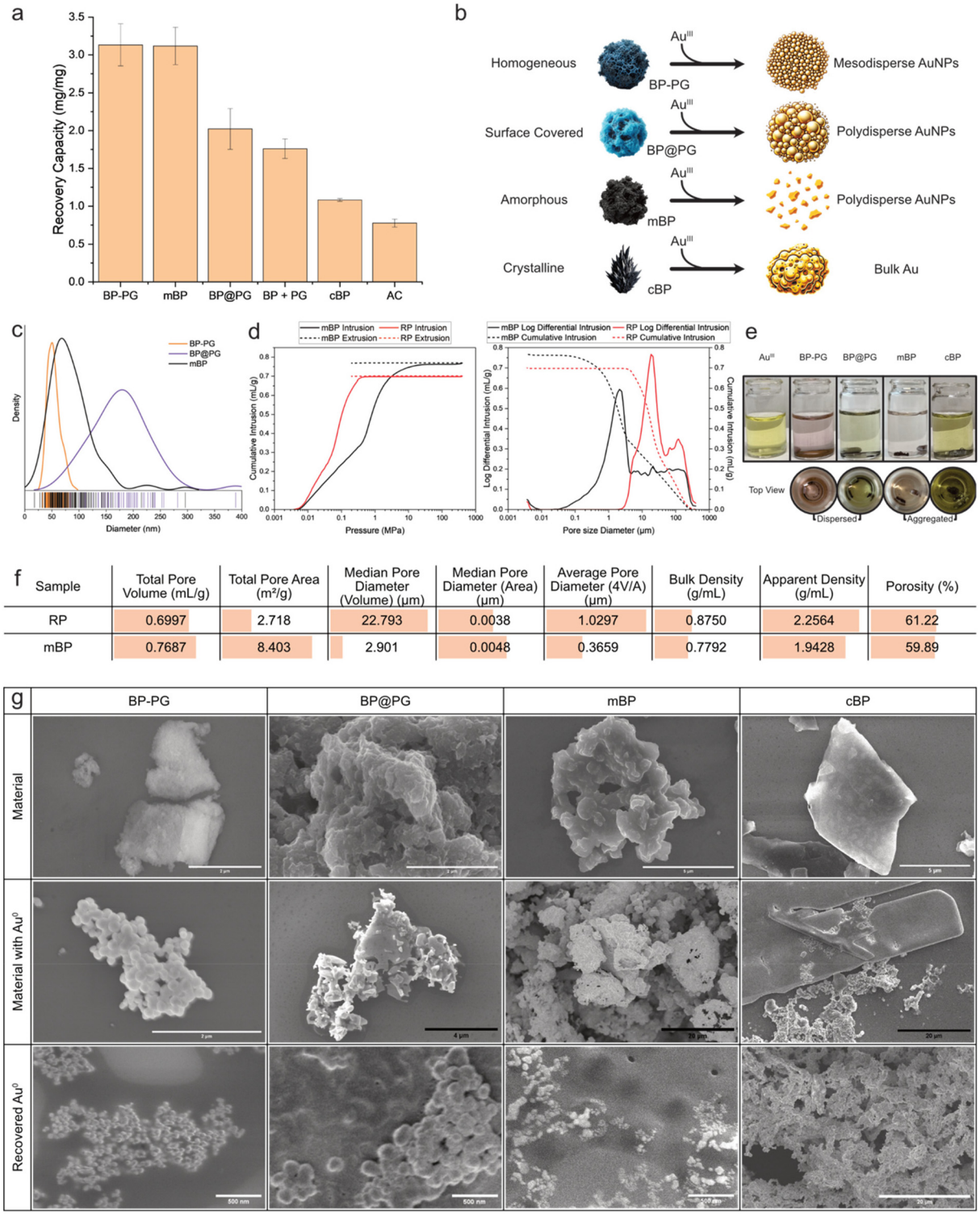

f

Sample	Total Pore Volume (mL/g)	Total Pore Area (m^2/g)	Median Pore Diameter (Volume) (μm)	Median Pore Diameter (Area) (μm)	Average Pore Diameter (4V/A) (μm)	Bulk Density (g/mL)	Apparent Density (g/mL)	Porosity (%)
RP	0.6997	2.718	22.793	0.0038	1.0297	0.8750	2.2564	61.22
mBP	0.7687	8.403	2.901	0.0048	0.3659	0.7792	1.9428	59.89

Fig. 5 (a) Au recovery capacity of BP–PG, mBP, BP@PG, BP + PG, cBP, and AC. (b) Scheme depicting the influence of the produced nanomaterials' impact on recovered Au^0 morphology. (c) Size distribution analysis of recovered Au^0 species derived from SEM micrographs. (d) Cumulative intrusion *vs.* pressure and log differential intrusion *vs.* pore size analysis of mBP. (e) Images of Au^{III} solutions after treatment with BP–PG, mBP, BP@PG, and cBP. (f) Hg porosimetry of RP and mBP. (g) SEM images of produced nanomaterials before and after treatment of EWL, and the Au^0 species after recovery. AI-generated nanomaterial image.

indicated by the more pronounced absorbance of UV-Vis radiation 15 min after dispersion of the nanomaterials (ESI 2e†). The very high dispersibility of BP–PG in aqueous environments is due to the high incorporation of the hydrophilic PG component into the nanohybrid in comparison to BP@PG, as revealed by thermogravimetric analysis (TGA) (Fig. 2m), as well as the negative surface charge (Fig. 2k). As indicated by the TGA data, ~30% of the total weight of BP–PG is attributed to the PG component, as compared to only ~10% for BP@PG. The high incorporation of both components, BP and PG (Fig. 2m), a solid material with a polymer, can be easily achieved mechanochemically, whereas the solvent-based approach fails to yield a nanohybrid with a balanced w/w ratio of the components. In the case of Au^{III} conversion to AuNP, the high degree of BP leads to high recovery capacity, whereas the high degree of PG leads to more AuNP stabilization. The advanced nanohybrid properties of BP–PG compared to BP@PG indicates a material that is highly functionalized, resulting in a robust incorporation of its components. This leads to a more homogeneous architecture with a uniform distribution of both BP and PG elements. Such a structure promises superior performance in applications that leverage the unique properties of both BP and PG, enhancing efficiency and effectiveness across a wide range of uses.

Selective reduction of gold ions to gold nanoparticles using BP–PG

As already mentioned, BP nanomaterials have recently been explored for their ability to selectively interact with certain metal ions in solution, such as Au^{III}, and to reduce them to zero-valent solids that precipitate out of solution.[14,15,58,59] BP–PG's ability to selectively recover Au^{III} in the form of AuNPs was tested against a simulated EWL (Fig. 4a) and was analyzed *via* scanning electron microscopy (SEM, Fig. 4b and c), atomic absorption spectroscopy (AAS, Fig. 4d), ultraviolet-visible spectroscopy (UV-Vis, Fig. 4g), and XPS (Fig. 4h).

BP–PG's selectivity towards metals most found in EWL was tested (Fig. 4d), specifically Au^{III}, Fe^{III}, Cu^{II}, Ni^{II}, Zn^{II}, and Cr^{III}, in acidic solutions (pH 1.0) as commonly derived from electronic waste. To concentrated metal chloride and nitrate solutions (0.5 mg mL^{-1} of each), BP–PG was added (1 mg mL^{-1}) and the mixtures were treated for 30 minutes before letting the nanoparticles sediment over 30 minutes, in which the supernatants were collected and analyzed by AAS. None of the metals apart from gold were reduced by BP–PG (Fig. 4d). To gain a mechanistic insight into the interaction between BP–PG and these metals, a cyclic voltammogram (CV) of a BP–PG dispersion was obtained (Fig. 4f) that reveals an irreversible oxidation of the phosphorus component from P^0 to P^{3+} and P^{5+}, which are finally converted to H_3PO_4, indicated by the peak at +630.4 mV *vs.* Ag/AgCl (or 835.4 *vs.* standard hydrogen electrode (SHE)).[49,60–62] As the reduction potential of $[AuCl_4]^-$ to zero-valent Au^0 is +1002 mV *vs.* SHE, which is higher than the work function of BP–PG (+835.0 mV *vs.* SHE), an electron transfer from BP–PG to $[AuCl_4]^-$ can occur spontaneously without the need of external energy/activation.[14,15,59] On the other hand, all other metal ions have work functions lower than that of BP–PG (Fig. 4e).[63] Therefore, an interaction between BP–PG and $[AuCl_4]^-$ leads to the formation of the redox pair BP–PG/$AuCl^{4-}$, where the BP–PG reduces the metal cation to the zero-valent state, thereby oxidizing the BP component of BP–PG. After treatment of EWL with BP–PG, the zero-valent gold is reduced onto BP–PG in the form of nanoparticles. The gold-loaded nanohybrid (AuNP@BP–PG, Fig. 4b and 5g) can sediment from the mixture within a short amount of time (<1 hour), which allows the transfer of the gold-free EWL to waste-water treatment. To recover the AuNPs from AuNP@BP–PG, the BP component can be oxidized to H_3PO_4. This can be done naturally under ambient conditions where the BP component is oxidized by oxygen or can be done on demand by using a stronger oxidizing agent such as hydrogen peroxide (Fig. 4i). In both cases, the degradation of the BP–PG nanoparticles will release the AuNPs to form a pink-red dispersion of gold nanoparticles (Fig. 4i and ESI 6†). SEM images show mesodisperse gold nanoparticles with a size of ~50 nm (Fig. 4c, 5d and g). UV-Vis analysis of these dispersions reveals the characteristic absorbance of gold nanoparticles at ~537 nm (Fig. 4g). High-resolution Au 4f XPS analysis indicates zero-valent Au^0 species, proving the reduction of Au^{III} to AuNP, as well as a small portion of Au^I species. Moreover, Cu 2p3/2 XPS analysis indicates adsorption of Cu ions onto the surface of BP–PG due to the known ability for copper-ions to interact with BP and oxidize it (ESI 5†), although only in negligible amounts as proven by AAS (Fig. 4d).[64] SEM images of the AuNPs derived from mBP reveal a non-uniform morphology (Fig. 5g), which may be a result of the lack of a stabilizing agent such as PG (Fig. 5b). This implies that composition of BP–PG is favorable for the formation of spherical mesodisperse gold nanoparticles which could be stabilized by the polymeric PG component.

Impact of material architecture on Au recovery

Typically, nanomaterials are produced at a high-cost due to the use of advanced production methodologies that yield materials with precisely defined and desirable properties.[65] However, in this case, the lower-cost mechanochemical approach leads to the formation of both a high-quality amorphous BP platform (mBP) and its subsequent mechanochemical functionalization, that results in a true nanohybrid (BP–PG) that outperforms a nanohybrid derived from a solvent-based procedure (BP@PG) in interactive applications, as demonstrated by the enhanced properties discussed above. Moreover, a homogeneous distribution of BP and PG within the BP–PG material should lead to a formation of a high-quality mesodisperse stabilized AuNPs, which are far more desirable than bulk gold due to their unique physicochemical properties that enable advanced applications in electronics, medicine, and catalysis.[66,67]

To validate this, the gold recovery capacity from EWL of mBP, cBP, BP–PG, BP@PG, BP + PG, and activated carbon (AC) was assessed (Fig. 5e). As mentioned earlier, mBP was used for the preparation of BP–PG, BP@PG, and BP + PG to achieve

comparable results. Specifically, amorphous mBP was compared to its expensive crystalline counterpart cBP, and BP–PG was compared to its expensive solvent-derived counterpart BP@PG. This comparison aimed to evaluate the impact of the materials' architectures on Au^{III} reduction. Both mechanochemically-derived BP–PG and mBP demonstrated the ability to reduce gold ions more than 3 times their weight—nearly triple the capacity of previously reported nanomaterials.[15,68–73]

A significant impact on the quality and the capacity of the produced Au^0 species is determined by the architecture and distribution of the reducing-agent (BP) and nanoparticle stabilizing polymer (PG) of a recovery platform (Fig. 5a, d, g and ESI 7†). Studies have shown that dendritic polyglycerol (dPG) can be used to stabilize and functionalize AuNPs, that enhances their dispersibility and stability in aqueous environments. The hydrophilic nature of polyglycerol improves the uniform distribution of AuNPs, preventing aggregation.[53] As the PG component in BP–PG is uniformly embedded within the BP component (Fig. 5a and g), mesodisperse AuNPs (<100 nm) are formed (Fig. 5d and g). On the other hand, the PG component in BP@PG is more separated by covering parts of the BP surface (Fig. 5a and g), that results in a lower Au recovery capacity (Fig. 5e). Also, with less PG in BP@PG (Fig. 2m), large polydisperse AuNPs are formed as shown in Fig. 5d and g. Without any PG to stabilize AuNPs in amorphous mBP, AuNPs with various morphologies are formed (Fig. 5g). Crystalline few-layered cBP nanoflakes produce less-desirable large non-dispersible bulk gold structures (Fig. 5g). The lower surface area attributed to a few-layer tightly stacked crystalline structure consequentially leads to a much lower recovery capacity by cBP (~1/3) as compared to mBP and BP–PG (Fig. 5e). It is crucial to highlight that the amorphous structure of the BP component in mBP, BP–PG, BP@PG, and BP + PG, confirmed by solid-state NMR spectroscopy (Fig. 2d) and PXRD analysis (ESI 1†), contributes to an increased surface area compared to the reported exfoliated BP two-dimensional nanoflakes. Thus, mercury intrusion porosimetry (MIP) measurements reveal a three-fold increase in the total pore area, or specific surface area (SSA), after mechanochemical treatment to 8.4 $m^2\ g^{-1}$ for mBP as compared to 2.7 $m^2\ g^{-1}$ for its precursor, RP (Fig. 5c, f and ESI 9†). Such a substantial SSA is beneficial for applications that rely on surface interactions, such as ion-reduction, catalysis, adsorption, and sensor technologies, as a higher SSA means more surface area is available for these interactions.[74,75] The increased porosity induced by HEPBM is advantageous for the nucleation and subsequent growth of gold nanoparticles (AuNPs), as these pores serve as primary seeding sites facilitating AuNP formation.[14,33] Moreover, the average pore diameter for mBP was decreased down to 0.366 μm from 1.03 μm for its RP precursor (Fig. 5f and ESI 9†). These small nanosized pores are favorable for the reduction of Au^{III} to small and highly-desirable AuNPs, as shown in Fig. 5g. Finally, the superior dispersibility of BP–PG, also attributed to the hydrophilic nature of PG, ensures uniform nanomaterial distribution in aqueous environments. This contrasts sharply with mBP's tendency to agglomerate, that reduces its dispersibility and complicating its application by necessitating additional steps to disperse it in aqueous systems (Fig. 5b and ESI 8†).

Palladium and platinum recovery

With respect to Pd and Pt, UV-Vis analysis of palladium(II) chloride and hexachloroplatinic acid before and after treatment with BP–PG both indicate interaction between BP–PG and the dissolved metal ions (ESI 10†). A stronger interaction seems to take place between Pd^{II} ions and BP–PG than with Pt^{IV} and BP–PG. The reduction potential of Pd^{II} (0.951 V *vs.* SHE) is higher than that of BP–PG's work function (0.835 V *vs.* SHE), allowing the formation of the BP–PG/Pd^{II} redox pair. On the other hand, the reduction potentials of $[PtCl_6]^{2-}$ and $[PtCl_4]^{2-}$ (0.680 V and 0.755 V *vs.* SHE, respectively) are slightly lower than BP–PG's work function. Hi-res XPS analysis of adsorbed Pt and Pd species suggests that in the case of Pt, Pt^{IV} ion adsorption onto BP–PG is dominant, whereas for Pd, reduction to Pd^0 is favored. This is further indicated by UV-Vis analysis.

Conclusion

Here, we demonstrate that the architecture of a multi-component black phosphorus nanohybrid plays a significant role in its interfacial capabilities. We achieved this by mechanochemical preparation of BP–PG in a ball-mill by a combination of an inorganic solid and an organic hydrophilic polymer, and showed its superior performance against a solvent-derived nanomaterial towards the selective reduction of gold ions from an ionic mixture. BP–PG, featuring an amorphous structure with high SSA and nanosized pores, can recover AuNPs exceeding 3 times its weight, a recovery capacity almost 3 times higher than other reported nanomaterials. The recovered Au^0 species are mesodisperse <100 nm AuNP's stabilized by the PG polymer. Furthermore, we polymerize glycidol, a low-functional liquid epoxide, to polyglycerol mechanochemically. In order to acquire such a nanohybrid, we utilized PBM for its ability to continuously generate fresh reactive surfaces through the peeling and recombination of the nanomaterial's components. This process results in a homogeneous architecture that is beneficial for interfacial applications, as compared to solvent-based approaches which generate surface coverage that hinders contact and the formation of AuNPs. Here, we observed the importance of addressing a material's distribution of its functional components for optimizing its performance in interfacial applications, thereby circumventing the need for expensive additional steps such as fixing the material onto porous high-surface-area materials like covalent organic frameworks. Moreover, such a procedure benefits from being able to generate high energies without the use of high temperatures, long reaction times, strenuous procedures, toxic solvents, and dangerous activation agents typically used for the functionalization of BP. This study underscores the importance of considering the synthetic approach of a nanohybrid,

how it affects its architecture, and how that in turn can influence its performance in applications where surface interactions are important, such as catalysis, adsorption, or ion-reduction.

Abbreviations

AC	Activated carbon
AAS	Atomic absorption spectroscopy
AuNP	Gold nanoparticle
AuNP@BP–PG	Gold-loaded black phosphorus–polyglycerol
BP	Black phosphorus
BP–PG	Black phosphorus–polyglycerol nanohybrid
BP@PG	Solvent polyglycerol-functionalized BP nanoparticles
BPR	Ball-to-powder ratio
cBP	Crystalline black phosphorus (*via* CVT)
CVT	Chemical vapor transport
CV	Cyclic voltammetry
DLS	Dynamic light scattering
dPG	Dendritic polyglycerol
EWL	Electronic waste leachate
FT-IR	Fourier transform infrared spectroscopy
(HE)PBM	(High-energy) planetary ball milling
MIP	Mercury intrusion porosimetry
mBP	Mechanochemically derived black phosphorus
NMP	*N*-Methyl-2-pyrrolidone
PG	Polyglycerol
PXRD	Powder X-ray diffraction
RP	Red phosphorus
SEM	Scanning electron microscopy
sBP	Solvothermally derived black phosphorus
SSA	Specific surface area
TGA	Thermogravimetric analysis
XPS	X-ray photoelectron spectroscopy
ZP	Zeta potential

Data availability

All data generated or analyzed during this study are included in this article and its ESI.†

Conflicts of interest

A patent was filed based on this study: European Patent Application Nr. 24 203 295.1.

Acknowledgements

We would like to acknowledge the assistance of the Core Facility BioSupraMol supported by the Deutsche Forschungsgemeinschaft (DFG). We also would like to acknowledge the contributed assistance of Jana Falkenhagen, Carsten Prinz, and Anett Myxa from the "Bundesanstalt für Materialforschung und -prüfung" (BAM) on the porosity analysis of samples and Dr Philip Nickl, Arun Krishnan V., and Nicholas Breitkreuz from the Freie Universität Berlin on the XPS analysis. Some illustrations in this manuscript were created with the assistance of ChatGPT, an AI-based tool developed by OpenAI. The authors reviewed and refined the AI-generated illustrations to ensure alignment with the manuscript's scientific content.

References

1 Ankit, L. Saha, V. Kumar, J. Tiwari, Sweta, S. Rawat, J. Singh and K. Bauddh, *Environ. Technol. Innovation*, 2021, **24**, 102049.
2 L. H. Xavier, M. Ottoni and L. P. P. Abreu, *Resour., Conserv. Recycl.*, 2023, **190**, 106840.
3 B. Lim and R. D. Alorro, *Sustainable Chem.*, 2021, **2**, 686–706.
4 N. Johansson, J. Krook, M. Eklund and B. Berglund, *J. Cleaner Prod.*, 2013, **55**, 35–44.
5 K. A. Hudson-Edwards, H. E. Jamieson and B. G. Lottermoser, *Elements*, 2011, **7**, 375–380.
6 B. G. Lottermoser, *Elements*, 2011, **7**, 405–410.
7 K. Binnemans, P. T. Jones, B. Blanpain, T. Van Gerven and Y. Pontikes, *J. Cleaner Prod.*, 2015, **99**, 17–38.
8 OECD, *Mining and Green Growth in the EECCA Region*, OECD, 2019.
9 S. A. Cotton, in *Chemistry of Precious Metals*, Springer Netherlands, Dordrecht, 1997.
10 F. Tesfaye, D. Lindberg, J. Hamuyuni, P. Taskinen and L. Hupa, *Miner. Eng.*, 2017, **111**, 209–221.
11 A. Ashiq, J. Kulkarni and M. Vithanage, in *Electronic Waste Management and Treatment Technology*, Elsevier, 2019, pp. 225–246.
12 L. Chang, Y. Cao, G. Fan, C. Li and W. Peng, *RSC Adv.*, 2019, **9**, 20226–20239.
13 M. Veselý, P. Marvan, J. Trejbal, V. Mazánek, J. Luxa, J. Šturala and Z. Sofer, *ACS Appl. Mater. Interfaces*, 2020, **12**, 22702–22709.
14 C. J. An, Y. H. Kang, C. Lee and S. Y. Cho, *Adv. Funct. Mater.*, 2018, **28**, 1800532.
15 S. Zhang, Q. Zhao, D. Wang, S. Deng, D. Li, X. Liu, S. Wu, X. Zhang and B. Xing, *ChemSusChem*, 2021, **14**, 2698–2703.
16 T. Chen, W. Zeng, C. Tie, M. Yu, H. Hao, Y. Deng, Q. Li, H. Zheng, M. Wu and L. Mei, *Bioact. Mater.*, 2022, **10**, 515–525.
17 S. Moschetto, A. Ienco, G. Manca, M. Serrano-Ruiz, M. Peruzzini, A. Mezzi, M. Brucale, M. Bolognesi and S. Toffanin, *Dalton Trans.*, 2021, **50**, 11610–11618.
18 J. Shao, H. Xie, H. Huang, Z. Li, Z. Sun, Y. Xu, Q. Xiao, X.-F. Yu, Y. Zhao, H. Zhang, H. Wang and P. K. Chu, *Nat. Commun.*, 2016, **7**, 12967.

19 J. O. Island, G. A. Steele, H. S. J. van der Zant and A. Castellanos-Gomez, *2D Mater.*, 2015, **2**, 011002.
20 R. Gao, X. Wang, X. Zhang, S. Zhang, X. Li, X.-F. Yu and L. Bai, *Sep. Purif. Technol.*, 2023, **316**, 123771.
21 S. Lange, P. Schmidt and T. Nilges, *Inorg. Chem.*, 2007, **46**, 4028–4035.
22 M. Köpf, N. Eckstein, D. Pfister, C. Grotz, I. Krüger, M. Greiwe, T. Hansen, H. Kohlmann and T. Nilges, *J. Cryst. Growth*, 2014, **405**, 6–10.
23 T. Nilges, M. Kersting and T. Pfeifer, *J. Solid State Chem.*, 2008, **181**, 1707–1711.
24 J. R. Brent, N. Savjani, E. A. Lewis, S. J. Haigh, D. J. Lewis and P. O'Brien, *Chem. Commun.*, 2014, **50**, 13338–13341.
25 Z. Guo, H. Zhang, S. Lu, Z. Wang, S. Tang, J. Shao, Z. Sun, H. Xie, H. Wang, X.-F. Yu and P. K. Chu, *Adv. Funct. Mater.*, 2015, **25**, 6996–7002.
26 O. Bawadkji, M. Cherri, A. Schäfer, S. Herziger, P. Nickl, K. Achazi, I. S. Donskyi, M. Adeli and R. Haag, *Adv. Mater. Interfaces*, 2022, 2201245.
27 A. Ozawa, M. Yamamoto, T. Tanabe, S. Hosokawa and T. Yoshida, *J. Mater. Chem. A*, 2020, **8**, 7368–7376.
28 S. Zhu, Q. Liang, Y. Xu, H. Fu and X. Xiao, *Eur. J. Inorg. Chem.*, 2020, **2020**, 773–779.
29 F. Luo, D. Wang, J. Zhang, X. Li, D. Liu, H. Li, M. Lu, X. Xie, L. Huang and W. Huang, *ACS Appl. Nano Mater.*, 2019, **2**, 3793–3801.
30 D. An, J. Fu, Z. Xie, C. Xing, B. Zhang, B. Wang and M. Qiu, *J. Mater. Chem. B*, 2020, **8**, 7076–7120.
31 Y. Zhang, C. Ma, J. Xie, H. Ågren and H. Zhang, *Adv. Mater.*, 2021, **33**, 2100113.
32 C. Sun, L. Wen, J. Zeng, Y. Wang, Q. Sun, L. Deng, C. Zhao and Z. Li, *Biomaterials*, 2016, **91**, 81–89.
33 T. S. Sreeprasad, P. Nguyen, N. Kim and V. Berry, *Nano Lett.*, 2013, **13**, 4434–4441.
34 Y. Zheng, X. Qi, F. Xiao, F. Wang and N. Wang, *Appl. Surf. Sci.*, 2023, **611**, 155723.
35 F. Xiao, R. Yu and N. Wang, *Appl. Surf. Sci.*, 2022, **604**, 154568.
36 A. Krusenbaum, S. Grätz, G. T. Tigineh, L. Borchardt and J. G. Kim, *Chem. Soc. Rev.*, 2022, **51**, 2873–2905.
37 J. L. Howard, Q. Cao and D. L. Browne, *Chem. Sci.*, 2018, **9**, 3080–3094.
38 C.-M. Park and H.-J. Sohn, *Adv. Mater.*, 2007, **19**, 2465–2468.
39 C. Ferrara, E. Vigo, B. Albini, P. Galinetto, C. Milanese, C. Tealdi, E. Quartarone, S. Passerini and P. Mustarelli, *ACS Appl. Energy Mater.*, 2019, **2**, 2794–2802.
40 S. V. Pedersen, F. Muramutsa, J. D. Wood, C. Husko, D. Estrada and B. J. Jaques, *npj 2D Mater. Appl.*, 2020, **4**, 36.
41 T. Ramireddy, T. Xing, M. M. Rahman, Y. Chen, Q. Dutercq, D. Gunzelmann and A. M. Glushenkov, *J. Mater. Chem. A*, 2015, **3**, 5572–5584.
42 I. Sultana, M. M. Rahman, T. Ramireddy, Y. Chen and A. M. Glushenkov, *J. Mater. Chem. A*, 2017, **5**, 23506–23512.
43 M. Nagao, A. Hayashi and M. Tatsumisago, *J. Power Sources*, 2011, **196**, 6902–6905.
44 J. Qian, D. Qiao, X. Ai, Y. Cao and H. Yang, *Chem. Commun.*, 2012, **48**, 8931–8933.
45 Y. Kim, Y. Park, A. Choi, N. Choi, J. Kim, J. Lee, J. H. Ryu, S. M. Oh and K. T. Lee, *Adv. Mater.*, 2013, **25**, 3045–3049.
46 F. Zhou, L. Ouyang, M. Zeng, J. Liu, H. Wang, H. Shao and M. Zhu, *J. Alloys Compd.*, 2019, **784**, 339–346.
47 G. Abellán, S. Wild, V. Lloret, N. Scheuschner, R. Gillen, U. Mundloch, J. Maultzsch, M. Varela, F. Hauke and A. Hirsch, *J. Am. Chem. Soc.*, 2017, **139**, 10432–10440.
48 X. Zhang, Z. Zhang, S. Zhang, D. Li, W. Ma, C. Ma, F. Wu, Q. Zhao, Q. Yan and B. Xing, *Small*, 2017, **13**, 1701210.
49 T. Zhang, Y. Wan, H. Xie, Y. Mu, P. Du, D. Wang, X. Wu, H. Ji and L. Wan, *J. Am. Chem. Soc.*, 2018, **140**, 7561–7567.
50 J. Park, A. Kim and B.-S. Kim, *Nat. Commun.*, 2023, **14**, 5855.
51 M. Roshith, T. G. S. Babu and D. V. Ravi Kumar, *AIP Conf. Proc.*, 2023, **2548**, 040004.
52 A. Sivo, I. Montanari, M. C. Ince and G. Vilé, *Green Chem.*, 2024, **26**, 7911–7918.
53 T. Bewersdorff, J. Vonnemann, A. Kanik, R. Haag and A. Haase, *Int. J. Nanomed.*, 2017, **12**, 2001–2019.
54 O. Bawadkji and R. Haag, *RSC Mech.*, 2024, **1**, 536–543.
55 E. J. Vandenberg, *J. Polym. Sci., Polym. Chem. Ed.*, 1985, **23**, 915–949.
56 L. Li, H. Wang, J. Ye, Y. Chen, R. Wang, D. Jin and Y. Liu, *Molecules*, 2022, **27**, 4408.
57 S. Kralj, M. Rojnik, R. Romih, M. Jagodič, J. Kos and D. Makovec, *J. Nanopart. Res.*, 2012, **14**, 1151.
58 J. Plutnar, Z. Sofer and M. Pumera, *RSC Adv.*, 2020, **10**, 36452–36458.
59 S.-Y. Cho, H.-J. Koh, H.-W. Yoo and H.-T. Jung, *Chem. Mater.*, 2017, **29**, 7197–7205.
60 L. Wang, Z. Sofer and M. Pumera, *ChemElectroChem*, 2015, **2**, 324–327.
61 R. Gusmão, Z. Sofer and M. Pumera, *ACS Nano*, 2018, **12**, 5666–5673.
62 S. Zhang, X. Zhang, L. Lei, X. Yu, J. Chen, C. Ma, F. Wu, Q. Zhao and B. Xing, *Angew. Chem., Int. Ed.*, 2019, **58**, 467–471.
63 *CRC Handbook of Chemistry and Physics*, ed. W. M. Haynes, CRC Press, 95th edn, 2014.
64 Z. Zhu, S. Yang, K. Lu, S. Dong, X. Sun, J. Zheng, S. Gao, W. Liu and L. Mao, *National Science Open*, 2024, **3**, 20230073.
65 G. Pandey and P. Jain, *Beni-Suef Univ. J. Basic Appl. Sci*, 2020, **9**, 63.
66 M. M. Ghobashy, S. A. Alkhursani, H. A. Alqahtani, T. K. Eldamhougy and M. Madani, *J. Mater. Sci. Eng. B*, 2024, **301**, 117191.
67 I. Hammami, N. M. Alabdallah, A. A. Jomaa and M. Kamoun, *J. King Saud Univ., Sci.*, 2021, **33**, 101560.
68 M. K. M. Z. Hyder and B. Ochiai, *Microsyst. Technol.*, 2018, **24**, 683–690.
69 T. S. Nguyen, Y. Hong, N. A. Dogan and C. T. Yavuz, *Chem. Mater.*, 2020, **32**, 5343–5349.

70 J. Kim, K. R. Kim, Y. Hong, S. Choi, C. T. Yavuz, J. W. Kim and Y. S. Nam, *ACS Appl. Mater. Interfaces*, 2019, **11**, 21915–21925.
71 S. Bratskaya, Y. Privar, A. Ustinov, Y. Azarova and A. Pestov, *Ind. Eng. Chem. Res.*, 2016, **55**, 10377–10385.
72 Z. Zhou, W. Zhong, K. Cui, Z. Zhuang, L. Li, L. Li, J. Bi and Y. Yu, *Chem. Commun.*, 2018, **54**, 9977–9980.
73 M. Mon, J. Ferrando-Soria, T. Grancha, F. R. Fortea-Pérez, J. Gascon, A. Leyva-Pérez, D. Armentano and E. Pardo, *J. Am. Chem. Soc.*, 2016, **138**, 7864–7867.
74 S. Głowniak, B. Szczęśniak, J. Choma and M. Jaroniec, *Molecules*, 2023, **28**, 2639.
75 J. Luo, X. Luo, Y. Gan, X. Xu, B. Xu, Z. Liu, C. Ding, Y. Cui and C. Sun, *Nanomaterials*, 2023, **13**, 2194.